RESEARCH ARTICLE

ADVANCED
PHYSICS
RESEARCH
Open Access

www.advphysicsres.com

Electronic Decoupling and Single-Molecule Charging of C$_{60}$ on h-BN/Rh(111)

Max Bommert, Gino Günzburger, Roland Widmer, Bruno Schuler, and Oliver Gröning*

A detailed understanding of the interaction between molecules and 2D materials is crucial to implement molecular films into next-generation 2D material-organic hybrid devices effectively. In this regard, energy level alignment and charge transfer processes are particularly relevant. This work investigates the interplay between a hexagonal boron nitride (h-BN) monolayer on an Rh(111) single crystal and self-assembled C$_{60}$ thin films. The influence of the corrugated topography and electrostatic surface potential originating from the h-BN/Rh(111) Moiré superstructure on the electronic level alignment and charging characteristics of C$_{60}$ is being studied. A combination of scanning tunneling microscopy/spectroscopy (STM/STS) and a theoretical tight-binding approach is used to gain insight into the C$_{60}$ bandstructure formation and electronic decoupling of specific C$_{60}$. This decoupling results from adsorption site-dependent variations of the molecular energy level alignment, which controls the strength of intermolecular hybridization. The decoupling of specific C$_{60}$ enables the direct observation of single-electron charging processes via STS and Kelvin probe force microscopy. The charging of the C$_{60}$ is enabled by combining two gating mechanisms: the electrostatic surface potential of the monolayer h-BN/Rh(111) Moiré and the electric field of the STM tip.

1. Introduction

After the groundbreaking isolation and electric characterization of graphene, scientific interest has quickly expanded to other 2D van der Waals (vdW) materials such as hexagonal boron nitride (h-BN), transition metal dichalcogenides, phosphorene, and silicene. Within this class of materials, we find intrinsically different electronic properties ranging from semimetallic to semiconducting and insulating, as well as more exotic properties such as superconductivity and edge conductivity in topological insulators.[1] In a constant pursuit to optimize and miniaturize electronic devices, the stacking of different 2D materials in vdW heterostructures leads to the creation of atomically thin field-effect transistors[2] and optoelectronic devices like solar cells.[3] However, despite the extensive collection of different 2D materials, tuning the properties for a specific application can be challenging. Interfacing 2D materials with organic molecular layers in a 2D-organic hybrid device opens up a pathway to diversify and optimize device performance, that is, by enhancing the photoresponse in phototransistors,[4] increasing the efficiency of polarized light-emitting diodes,[5] facilitating flexible electronics[6] or controlling interfacial energy barriers in semiconductor junctions.[7] Moreover, organic molecules can be tailor-made for a specific application, and fabrication can be scaled up at a low cost.[8]

Within the framework of this study, we focus on the interactions between epitaxial monolayer h-BN and the fullerene C$_{60}$ molecules. With its property to act as an efficient electron acceptor and its manifold chemical functionalization, C$_{60}$ is a crucial component in organic electronic devices.[9] On the other hand, h-BN has emerged among 2D materials as the ideal insulator due to its large electronic bandgap,[10] low concentration of trapped charges,[11] chemical inertness, and low permeability.[12] In recent years, numerous applications of h-BN were reported, for example, as an electrocatalyst for chemical reactions[13] or as a platform to study organic molecules decoupled from underlying substrates.[14] The creation of single layers of h-BN can be achieved either *via* mechanical exfoliation or self-limited growth by the decomposition of borazine (B$_3$N$_3$H$_6$) gas on hot metal single-crystal surfaces.[15] In the latter case, the type of metal substrate and the surface orientation can have large influences on the topography and electronic properties of the h-BN, as can be seen in the highly regular superstructure formed in the h-BN on Rh(111) material system.[16] Experiments combining h-BN/Rh(111) with different organic molecules revealed the potential of this material system as a platform to investigate individual molecules electronically decoupled from the underlying metal surface[14,17–19] to tune the molecular orbital level alignment[14] and to serve as a template for on-surface chemical

M. Bommert, G. Günzburger, R. Widmer, B. Schuler, O. Gröning
Empa
Swiss Federal Laboratories for Materials Science and Technology
Nanotech@Surfaces Laboratory
Dübendorf 8600, Switzerland
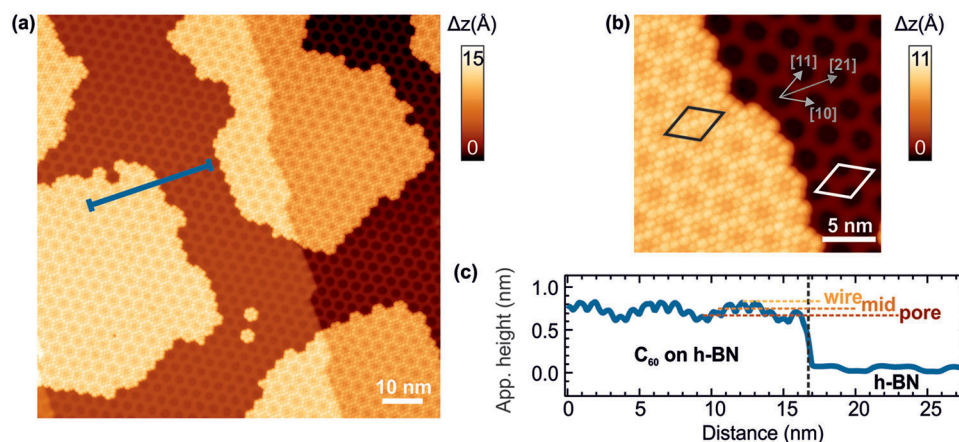E-mail: oliver.groening@empa.ch

Figure 1. Overview of the C_{60} h-BN/Rh(111) system. a) STM topography of C_{60} islands formed on the h-BN/Rh(111) Moiré (setpoint: −0.5 V, 40 pA). b) STM image of the C_{60} hexagonal adsorption configuration. The unit cell of h-BN/Rh(111) Moiré and C_{60} hexagonal adsorption configuration indicated in black and white respectively. Directions of the C_{60} lattice [21] and the Moiré [10],[11] indicated in grey (set point −0.5 V, 40 pA). c) Height profile along the blue line in (a). The three different apparent adsorption heights are indicated: C_{60} in the pore center, at an intermediate position (mid), and on top of a wire.

reactions, for instance, the growth of graphene *via* chemical vapor deposition.[20] Nowadays, it is well established that the superstructure consists of a Moiré lattice containing 12 × 12 Rh(111) and 13 × 13 BN unit cells.[16,21–23] The so-called "hole" and "wire" regions of the Moiré have different work functions resulting in a periodic electrostatic potential modulation and strong lateral electric fields.[19]

The adsorption configuration of C_{60} molecules on the h-BN/Rh(111) Moiré has been reported before.[15] However, the influence of Moiré's locally varying electrostatic surface potential on the electronic properties of the C_{60} layer has not been reported yet. While most molecules studied on h-BN/Rh(111) tend to be separated and adsorb mainly at the rim of individual Moiré pores, C_{60} forms close-packed molecular islands, leading to an extended electronic system formed by the π-π orbital overlap. In the following, we use a combination of scanning tunneling microscopy (STM) and spectroscopy (STS), Kelvin probe force spectroscopy (KPFS), and non-contact atomic force microscopy (nc-AFM) to investigate the effects of the electrostatic surface potential on energy level alignment, intermolecular hybridization, and charge transfer.

2. Results and Discussion

2.1. Adsorption Configuration

An overview STM image of a sub-monolayer coverage of C_{60} on the h-BN/Rh(111) Moiré is shown in **Figure 1**a. To ensure high C_{60} mobility and thus large C_{60} island formation, we kept the h-BN/Rh(111) surface at 100 °C during molecule deposition. Under these conditions, the C_{60} molecules aggregate and form close-packed 2D islands with a highly regular hexagonal adsorption configuration where the C_{60} rows are oriented along the [21] direction of the Moiré. Occasionally, other orientations can be observed, for example, in the upper left corner of Figure 1a. These 30° misoriented islands seem linked to step edge-induced nu-

cleation. For the aligned C_{60} islands, we observe a nearly perfect commensurability with the h-BN/Rh(111) Moiré, which imprints a $\sqrt{12} \times \sqrt{12}$ R30° superstructure on the molecular lattice. From the STM images, we determine an intermolecular distance between neighboring fullerenes of $d_{C60} = 0.95 \pm 0.04$ nm. Within the error margin, this agrees well with the $\sqrt{12} \times \sqrt{12}$ R30° superstructure as the 3.22 nm periodicity of the Moiré[16] translates into an in-plane intermolecular distance of 3.22 nm/$\sqrt{12}$ = 0.93 nm. The unit cells of the C_{60} structure and the Moiré are shown in the STM zoom-in (Figure 1b) in black and white, respectively. This indicates that the h-BN/Rh(111) template forces the C_{60} layer to exhibit substantial compressive stress of about 7% as compared to bulk C_{60} crystal.[24] Also, the out-of-plane z-corrugation of the C_{60} layer of about 1.7 Å (Figure 1c) does not significantly relax this strain. It increases the in-plane molecule-molecule distance by just about 0.5%.

As a result of the near-perfect commensurability, the majority of the adsorbed C_{60} molecules have three well-defined adsorption positions with respect to the Moiré pore center: one C_{60} in the pore center, six C_{60} surrounding it forming the intermediate shell at the Moiré pore rim and 12 C_{60} on the outer shell on top of the Moiré wires. The most common defects in the C_{60} islands are 1D stacking faults that appear regularly after 6 ± 1 filled pores shown in Figure S1, Supporting Information. The formation of these stacking faults might be a direct result of releasing the strain in the structure. The smallest aggregates of C_{60} found outside the molecular islands consist of seven C_{60}, and no individual or smaller-sized clusters are observed. This heptamer unit contains one C_{60} in the pore center and six C_{60} molecules at an intermediate position between pore and wire. Compared to the fully developed hexagonal phase, the heptamer lacks the outer hexagon of twelve C_{60} on the wire. As a result of the missing coordination, the heptamers intermediate C_{60} relax toward the wire and are located at a distance of 1.04 ± 0.04 nm from the pore center. A schematic of the two adsorption configurations with respect to the h-BN/Rh(111) superstructure is shown in **Figure 2**a.
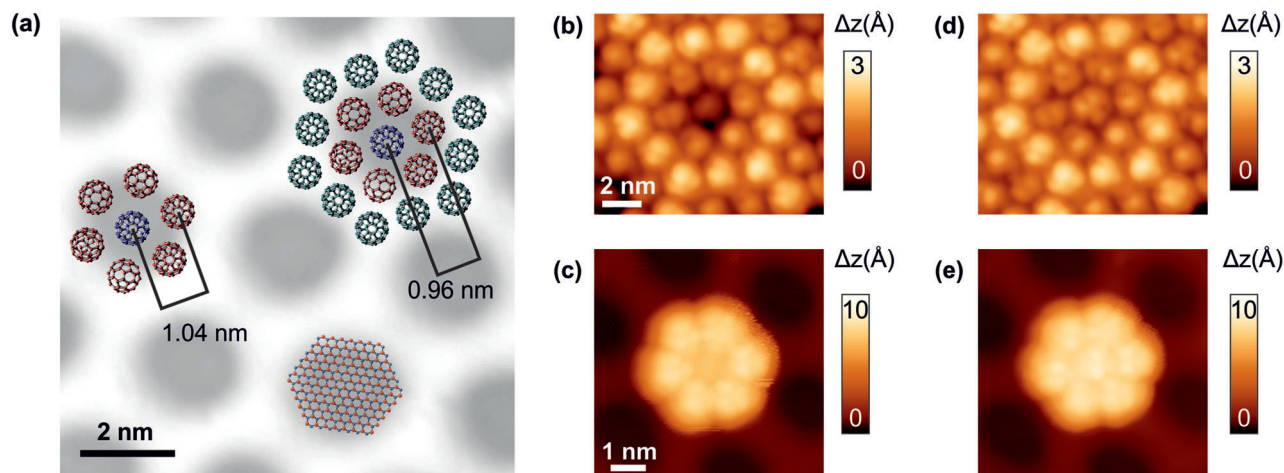
Figure 2. C_{60} adsorption positions on the Moiré. a) STM topography of bare h-BN/Rh(111) with a schematic of the C_{60} adsorption positions and underlying h-BN atomic structure (setpoint: −0.5 V, 40 pA). b) STM topography of a Moiré pore covered by C_{60} in hexagonal adsorption configuration (setpoint: −0.5 V, 10 pA). c) STM topography of a C_{60} heptamer (setpoint: −0.5 V, 3 pA). d,e) STM topography after tip-induced manipulation of central C_{60}.

By achieving intramolecular resolution in the STM, we could identify the orientation of the individual C_{60} through their orbital contrasts. We find C_{60} showing one, two, or three lobes corresponding to C_{60} in orientations where a hexagon-pentagon, hexagon-hexagon, or hexagon faces the STM tip. The molecular contrast is typical for the appearance of C_{60} in STM imaging and has been extensively studied.[25–28] In contrast to the high regularity of the adsorption configuration, the adsorption orientation of individual C_{60} is disordered, as seen in the STM image in Figure 2b. An STM image of the heptamer unit is shown in Figure 2c. Adsorption studies on different molecules on h-BN/Rh(111) (copper phthalocyanines,[19] naphthalocyanines,[16] and water molecules[14]) show a strongly modulated molecule-substrate interaction resulting in a significant templating effect that confines individual molecules in the pore regions of the Moiré structure. In contrast, we do not find C_{60} incorporated in larger islands, pointing to a dominant molecule-molecule interaction for the fullerenes.

We observe a peculiarity regarding the STM appearance of the center molecule. A voltage pulse or scanning at a setpoint larger than ± 1.5 V changes the apparent height of the central C_{60}. This manipulation is irreversible. After manipulation, the apparent height of the central molecule is increased and appears level with the molecules of the intermediate shell surrounding it. The manipulation effect on the island and heptamer is shown in the STM images in Figure 2d,e. We can observe an evident change in the manipulated molecules' orientation. We find a similar behavior for C_{60} adsorbed on h-BN/Ni(111). The work function of the h-BN/Rh(111) pore and the flat h-BN/Ni(111) are very similar: 3.6[19] and 3.55 eV,[29] respectively. We propose that for certain C_{60} orientations, the charge transfer from the substrate to the molecule is large enough to (partially) charge the C_{60}. The C_{60} orientation is changed upon manipulation, and thus the charge transfer is reduced. The investigations on C_{60} on h-BN/Ni(111) supporting this view will be published separately, and all further presented measurements are after the irreversible manipulation of the central molecule.

2.2. Adsorption-Site Dependent Gating of C_{60}

As discussed above, the topographic corrugation of the h-BN/Rh(111) superstructure results in an apparent height modulation of the C_{60} islands. The origin of this corrugation is found in the different bonding strengths between BN and Rh atoms depending on their adsorption position, that is, their registry with the underlying Rh atoms.[21] The distance between h-BN and rhodium strongly impacts the electronic structure as the BN in the pores hybridizes stronger with the rhodium substrate compared to the BN units in the wire regions. In turn, this results in different work functions for pore (3.6 eV) and wire (4.1 eV) regions.[19] The large change in the local vacuum level over a small ≈ 1 nm distance leads to strong lateral electric fields with the same periodicity as the corrugation. We used low-temperature STS measurements to probe the effect of this surface potential variation on the local density of states (LDOS) of the C_{60} molecules. **Figure 3**a depicts a dI/dV point spectrum of a C_{60} in a pore center within the hexagonal adsorption configuration. The most prominent feature in the positive range of the differential conductance is visible at 0.21 eV and can be attributed to the lowest unoccupied molecular orbital (LUMO) of the central C_{60}.

A series of equidistant dI/dV point spectra across the large island hexagonal configuration (top) and the heptamer cluster (bottom) is presented as a position-sample bias intensity plot in Figure 3b. In the hexagonal configuration (top part of Figure 3b), the LUMO of the C_{60} rigidly shifts from 0.21 to 0.33 to 0.76 eV for central, intermediate, and outer C_{60}, respectively. In the heptamer cluster (bottom part of Figure 3b), the LUMO shifts from 0.20 eV for the central C_{60} to 0.52 eV for the outer C_{60}. Notably, we find deviations of the LUMO energies of $\approx \pm 100$ meV for different C_{60} at the same adsorption position with respect to the Moiré. An example of this deviation can be seen when comparing the onset of the LUMO of molecules (1) and (5), shown in Figure 3b. The variations of the LUMO energy might be linked to the random rotational adsorption orientation of the C_{60}.
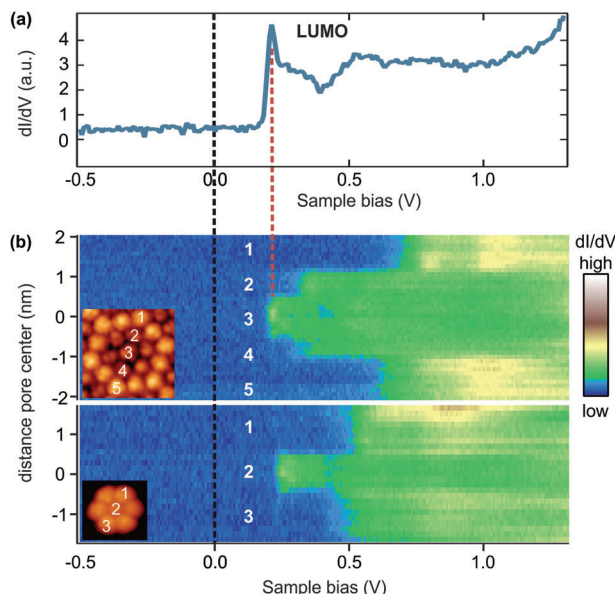
2300029 (3 of 9)

**ADVANCED
SCIENCE NEWS**

www.advancedsciencenews.com

**ADVANCED
PHYSICS
RESEARCH**
Open Access

www.advphysicsres.com

Figure 3. Adsorption position-dependent C_{60} LUMO energy. a) dI/dV point spectrum of a central C_{60} in a hexagonal adsorption configuration with the LUMO at 0.21 eV (setpoint: 1.5 V, 100 pA). b) dI/dV point spectra measured along a hexagonal (top) and heptamer (bottom) adsorption configuration shown in the insets. The C_{60} LUMO shifts rigidly to higher energies with increasing distance to the pore center (setpoint: 1.5 V, 100 pA).

The shift in LUMO energy as a function of the pore registry can be attributed to the spatial variations of the electrostatic surface potential in the pore center compared to the wire. Accordingly, we can use the LUMO energy of the C_{60} as a probe for the magnitude of the electrostatic surface potential. Smaller shifts—due to a weaker surface potential variation—of the orbital alignment have been reported for phthalocyanines on the h-BN/Cu(111) Moiré.[29] Due to the near-perfect commensurability of the C_{60}'s close-packed adsorption configuration, we can use the LUMO shift to probe the electrostatic surface potential at four distinct positions: first, the central C_{60}, second the six equivalent C_{60} at the intermediate shell of the large hexagonal island, third the six equivalent C_{60} at the outer shell of the heptamer and last the 12 C_{60} on the outer shell of the large hexagonal island. Geometrically there is a difference for the outer shell C_{60} whether they adsorb on the wire corner or in the middle of the wire; however, we do not find a significant difference in their LUMO level alignment. In the following, we compare how much the LUMO energy shifts compared to the central C_{60}. The maximum energy shift of 0.55 eV is found between the central C_{60} and the C_{60} in the outer shell on top of the wire. Our results agree with previously reported DFT calculations[30] for the h-BN/Rh(111) electrostatic potential. The slight difference in adsorption position between the intermediate shell C_{60} of the large hexagonal island and the outer shell of the C_{60} heptamer is enough to result in a significant difference in the LUMO shift, $\Delta E = 0.12$ eV and $\Delta E = 0.32$ eV, respectively. These observations indicate that the LUMO energy change from the central C_{60} to the C_{60} molecules on the rim is highly nonlinear. We find that the change of the LUMO energy in the large hexagonal island between the outer and intermediate shell ($\Delta E =$

0.43 eV) is three and a half times larger than the change between the intermediate shell and central C_{60} ($\Delta E = 0.12$ eV). Our findings corroborate the theoretically predicted profile of the work function change, which predicts a steep increase of the electrostatic surface potential 0.7 nm outside of the pore center. Thus we can confirm the theoretical calculations[19] of a larger electric field gradient at the pore rim. Additionally, this supports the suggested relation between the maximum surface electric field and preferred adsorption position, that is, trapping 2D, polarizable molecules at the pore rim.[14,19]

2.3. Electronic Decoupling

For an ideal gas-phase C_{60} molecule, one would expect a single LUMO peak consisting of three degenerate t_{1u} orbitals.[31] However, the results of other groups[32,33] and our findings reveal a more complex LUMO line shape in STS measurements for C_{60} adsorbed on surfaces, which appears to consist of multiple contributions. Due to the intricacy of the C_{60} LUMO line shape, multiple groups put effort into understanding the origin of the contributions to the LUMO line shape and the influence of different external factors such as substrate C_{60} interaction,[34,35] interaction with neighboring C_{60},[36,27] and inelastic electron-phonon scattering.[37,38] Nevertheless, the full extent of the external influences is not fully understood, and finding a universal understanding is challenging, mainly because different substrates can lead to different expressions of the interaction effects. The molecule-substrate interactions can be reduced by using substrates with a low density of states close to the Fermi level, for example, 2D materials or decoupling layers like graphene or h-BN.[39] The resulting decoupling can lead to LUMO-related STS orbital features with a width upward of 500 meV, as shown for a monolayer (ML) C_{60} on black phosphorus[40] and ML C_{60} on h-BN/Rh(110).[41] The h-BN/Rh(111) system can be expected to have similar properties in preventing molecule-substrate interaction. However, in our STS measurements, we consistently observe an extremely narrow STS signature of the LUMO-related orbital with roughly 70 meV FWHM (and a shoulder to higher energy) for C_{60} adsorbed in the pore center and a significantly broader width for the LUMO of the surrounding C_{60}. The sharpening of the LUMO for the central C_{60} appears to be independent of the C_{60}'s adsorption orientation and is found for both the heptamer unit and the fully developed hexagonal island. The corresponding experimental STS spectra of the LUMO for the center and outer C_{60} of the heptamer are shown in **Figure 4**a.

The difference between other decoupling materials can be found in the strong modulation of the h-BN/Rh(111) surface potential and the resulting LUMO energy adsorption position dependency. To understand the origin of the sharpened LUMO linewidth of the central C_{60}, we simulated the C_{60} electronic band structure with a tight-binding (TB) model adapted to the hBN/Rh(111) electrostatic surface potential. As the basis for the TB calculations of the heptamer unit, we used the randomly oriented C_{60} configurations in Figure 4b. In our calculations, we progressively vary the value for the electrostatic potential difference ΔeV_{SP} of the central (blue) C_{60} compared to the outer (red) C_{60}. The evolution of the LUMO-related LDOS for $\Delta eV_{SP} = 0$ to 300 meV for the central molecule (Figure 4c-i) and an outer
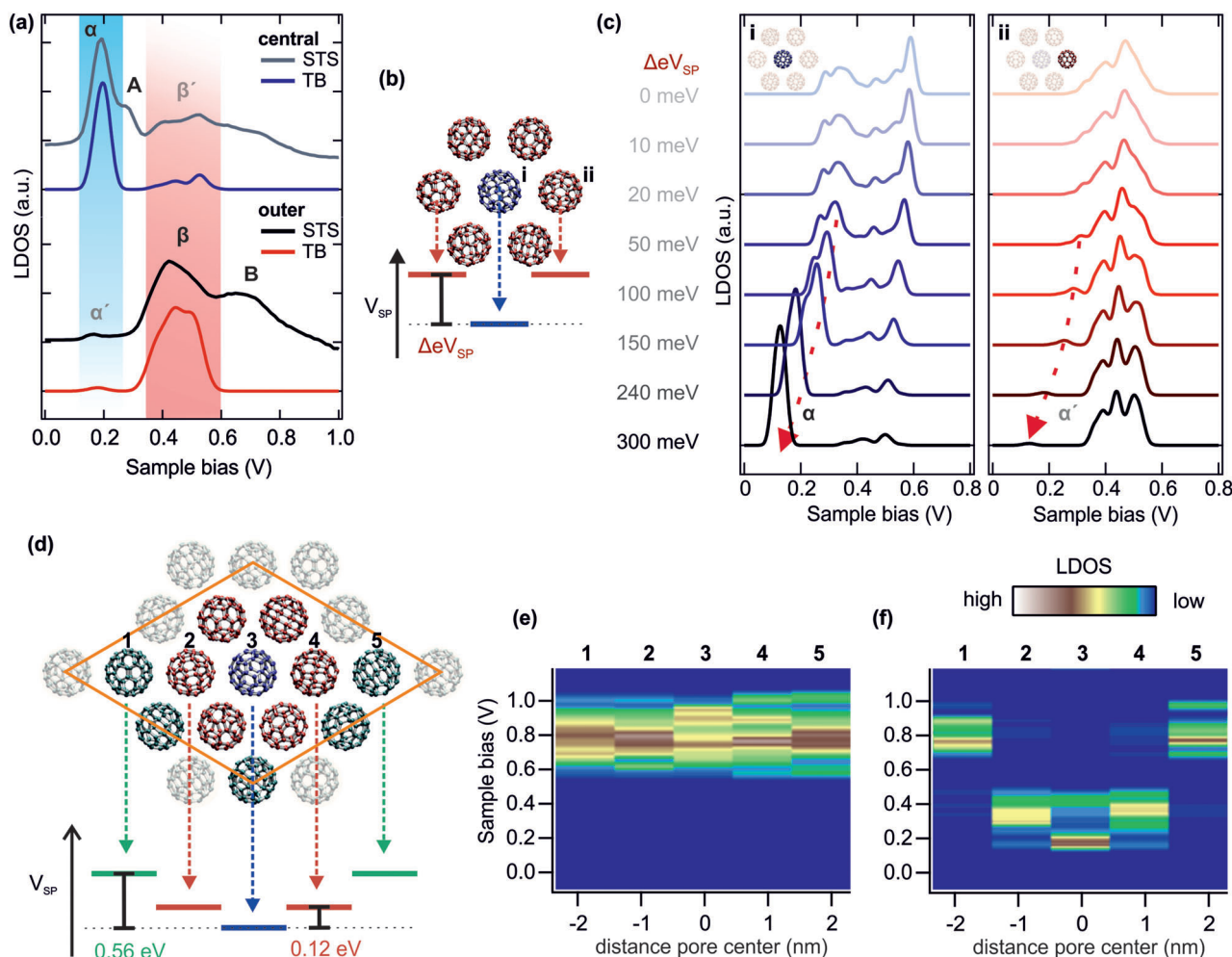
**ADVANCED
SCIENCE NEWS**

www.advancedsciencenews.com

**ADVANCED
PHYSICS
RESEARCH**
Open Access

www.advphysicsres.com

Figure 4. Modeling of the LUMO resonances. a) Comparison between dI/dV measurements (grey central, black outer C_{60}) and TB calculations (blue central, red outer C_{60}, ΔeV_{SP} =240 meV). Contributions to the LDOS of the central (outer) C_{60} via nearest neighbor hybridization indicated via red (blue) areas. A broadening of 80 meV was included in the calculations to reproduce the experimental data. b) Schematic of a C_{60} heptamer unit with a random C_{60} adsorption orientation. Energy diagram for electrostatic surface potential difference ΔeV_{SP} between central C_{60} (blue) and outer C_{60} (red). c) TB calculations of the LDOS for the configuration in (b) at varying ΔeV_{SP} for i) central and ii) outer C_{60}. As ΔeV_{SP} increases, the main LDOS contribution of the central C_{60} α and the contribution of the central C_{60} to the outer LDOS α' (red arrows) shift toward Fermi. d) Schematic of C_{60} unit cell used for the TB calculations of the hexagonal configuration. The unit cell is shown in orange and molecules not included in the unit cell are greyed out. The electrostatic surface potential differences with respect to the central C_{60} (blue) are indicated for the intermediate (red) and outer (green) molecules. e) LDOS for the molecules 1–5 indicated in (d) for no potential difference and f) for the potential differences depicted in the energy diagram in (d).

molecule (Figure 4c-ii) show inherently different line shapes as well as ΔeV_{SP} dependences. We find that the LUMO line shape is influenced by the rotation of the C_{60}, the number of neighboring molecules, and the energy level alignment of the neighboring C_{60}. While the C_{60}'s rotation plays a role in determining the exact line shape, the general trend of sharpening LUMO of the central C_{60} remains. Simulations for 100 different C_{60} rotations are presented in Figure S3, Supporting Information. The influence of the number of neighboring molecules can be seen when comparing the central and outer C_{60} LUMO at ΔeV_{SP} = 0 meV: a more complex and broader line shape for the central C_{60} with six neighboring molecules compared to a sharper line shape for the outer C_{60} with only three nearest neighbors. Looking at the LDOS of the central C_{60}, as ΔeV_{SP} increases, a single contribution labeled α increases in intensity and shifts with ΔeV_{SP} toward

Fermi energy while the rest of the peak's intensity decreases to the point where it nearly vanishes. A similar shift toward Fermi can be seen for the α' contribution of the LDOS of the outer C_{60}. However, the intensity of α' decreases with increasing ΔeV_{SP}. From this, we conclude that the hybridization between neighboring molecules can significantly influence the spectral line shape of the LDOS observed in STS. We can identify α' as a contribution of the central C_{60} to the LDOS of the outer C_{60}. The reverse hybridization, that is, the contribution of the outer C_{60} LDOS to the central C_{60} LDOS, cannot be as easily distinguished due to the increased number (six) of outer C_{60}.

To further understand which part of the measured LDOS can be attributed to hybridization, we compare our dI/dV point spectra to TB calculations for potential energy differences (ΔeV_{SP} = 240 meV) comparable to the h-BN/Rh(111) Moiré electrostatic

surface potential (Figure 4a). Note that the difference between central and outer LUMO is 240 meV compared to the 320 meV shown in the STS measurements in Figure 3b. The LUMO energy is sensitive to the orientation and adsorption position of the C_{60}. Previously mentioned α and α' contributions in the TB calculations are in excellent agreement with our experimental data. Due to the high energy resolution of the dI/dV spectra, we can also link a cluster of peaks β to the main contribution of the outer C_{60} and their respective hybridized counterparts on the central LDOS β'.

Our TB calculations agree with the experimental data within the red and blue shaded areas of Figure 4a. However, our dI/dV measurements show side peaks labeled A and B to the α and β that the TB model does not reproduce. The energy splitting between α and A is 87 meV which matches the energy of reported inelastic electron-phonon scattering on the Jahn-Teller active mode $H_g(3)$.[37] So far, this scattering process has only been observed in off-resonance electron tunneling through the C_{60} due to the small phonon energy.[38] The narrow linewidth of our dI/dV data allows us to distinguish such small energy splittings resonantly. To our knowledge, the only resonant electron-phonon scattering observed in C_{60} layers is with the phonon sideband at 210 meV, fitting well with the energy difference between β and B.[38]

We also studied theoretically the effect of intermolecular hybridization for randomly oriented C_{60} in the fully developed hexagonal layer shown in Figure 4d. The influence of the adsorption orientation on the hybridization becomes apparent in Figure 4e, where no potential difference is applied to the C_{60} in the unit cell. Due to the orientational disorder, we can see a comparable linewidth but a variable intensity distribution in the LUMO for different molecules. Figure 4f shows the LUMO of the same adsorption configuration, but we decrease the potential by 0.56 and 0.44 eV for the central and intermediate C_{60}, respectively. We chose the potential differences to match our experimental data in Figure 3b for the surface potential of the Moiré. Depending on the sites of the C_{60} (outer, intermediate, or central), the LUMO energy decreases accordingly. Hybridization of central-intermediate and intermediate-outer C_{60} is still visible but reduced for the intermediate-outer situation. It is noteworthy that compared to the heptamer case, where a potential difference of 240 meV between central C_{60} and surrounding C_{60} was assumed, here, this difference is only 120 meV. Still, the sharpening of the LUMO for the central C_{60} is very apparent.

We can conclude that the central C_{60} in both the heptamer and the hexagonal island is not only electronically isolated from the Rh(111) substrate by the h-BN layer but also from neighboring molecules by substrate-induced differences of the molecular orbital level alignment. The sharp LUMO of the central C_{60} we observe in STS and simulate in our TB calculations consists nearly exclusively of a single peak (α) which is very similar to the expected LDOS of an isolated ideal gas-phase C_{60}.

2.4. STM Tip-Induced Charging

The combined electronic decoupling of the substrate and the neighboring molecules is the foundation for observing an STM tip-induced charge transfer to the central C_{60}. Further increasing

the range of our STS measurements (**Figure 5**a) reveals next to the previously discussed LUMO at around 0.2 V additional features at −1.4 and 1.5 V for a central C_{60} in the large hexagonal island. In the unoccupied spectrum region at about 1.5 V, we observe a resonance with a similar line shape as LUMO. This resonance shifts analogous to the LUMO with the varying surface potential and maintains a constant energy difference of 1.3 eV to the LUMO. We can ascribe this positive bias feature to LUMO+1, matching previously reported experiments.[34,36] Analog to the LUMO, we find the sharpening of the orbital linewidth for the central C_{60}. However, the bias voltage and shape of the negative feature do not agree with reported values for the C_{60} electronic bandgap (e.g., 2.7 eV on Au(111)[34] and Au(887)[36] and 2.88 eV on black phosphorus[40]). The electronic bandgap is even larger on systems that shield the C_{60} from the substrate, for example, 3.5 eV on ML graphene on SiC.[35] Concluding from this, we can discard the possibility that the feature at −1.4 eV is the highest occupied molecular orbital (HOMO). Instead, we link it to an additional tunneling channel opening upon charging the C_{60}. Similar observations of charging peaks in the dI/dV signal have been reported for impurities in semiconductors[42,43] and molecules[14] if, as in the case of the central C_{60}, a molecular orbital is close to Fermi. To confirm this hypothesis, we performed KPFS (Figure 5a) on the same C_{60}, where the dI/dV spectrum was measured to gain more information on the suspected charging process. The electrostatic force between the tip and molecule changes when the molecule's charge state changes. The subsequent change in the tip's resonance frequency produces a sharp dip in the Kelvin force parabola[44,45] and is observed at the same voltage as the dI/dV spectra peak. Measuring different C_{60} adsorbed in the pore center, we find that the bias of the dI/dV peak, that is, dip in the KPFS parabola eV_C can vary between −1.1 and −2.1 V. The charging voltage is linearly dependent on the LUMO energy eV_{LUMO} via: $−a \cdot eV_C = eV_{LUMO}$. Here, a is the capacitive coupling of the tip voltage and the energy shift of the LUMO orbital lever arm, that is, the sample voltage drop over the molecule.[14] Due to the voltage drop over the molecule, the relatively small variations we find for $eV_{LUMO} = 0.24 \pm 0.1$ eV of the central C_{60} translate to the large variability of $eV_C = 1.6 \pm 0.5$ eV of the charging peak. Keeping in mind that the charging voltage is not only dependent on eV_{LUMO} but also scales linearly with the distance between STM-tip and sample we can make an estimate for the voltage drop across the molecule $a \approx 0.15$.

We can look at the combined STM-tip C_{60} h-hBN/Rh(111) system as a single molecular transistor with two capacitively coupled gating electrodes—the electrostatic surface potential of the h-BN/Rh(111) Moiré which varies with position and the electric field of the STM tip. The corresponding equivalent electric circuit is shown schematically in Figure 5b. With the surface potential fixed to the three adsorption positions, our variable gating via the STM tip allows the precise tuning between the two charge states, C_{60} and C_{60}^-. A schematic of the energetics of the charging process is shown in Figure 5c. In part (i), we consider the case of the free C_{60} in a vacuum, where Fermi lies between LUMO and HOMO. Upon adsorption on the h-BN/Rh(111) surface in part (ii) and formation of the hexagonal island, we find three dominant energy level alignments. The LUMO of the C_{60} in the pore center is gated by the surface potential to close proximity of the
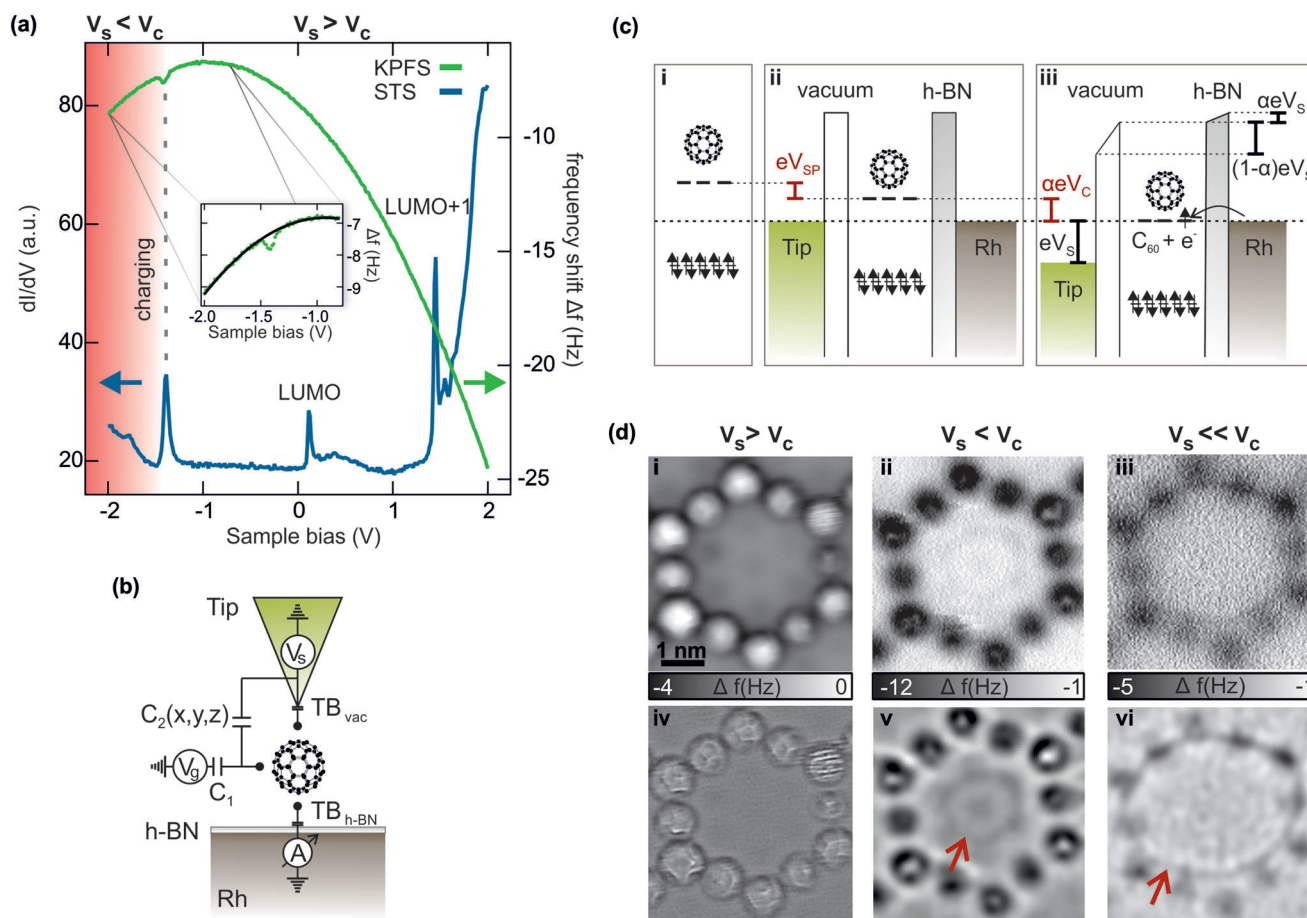
Figure 5. Charging of C_{60} adsorbed in the Moiré pore center. a) STS (blue) and KPFS (green) of central C_{60} in hexagonal configuration. Features in STS from left to right: charging peak, LUMO, and LUMO+1. Dip in the KPFS parabola at the same sample bias as the charging peak. Inset: fit (black) of KPFS data (green dots) (setpoint STS: 1.5 V, 150 pA, KPFS: 1.5 V, 150 pA, excitation amplitude: 36 pm, Q-factor: 27k). b) Schematic of a C_{60} single molecular transistor with a combination of gating effects via capacitive coupling of the electrostatic surface potential and the electric field of the STM tip. c) Energy level diagram for i) isolated C_{60}, ii) C_{60} on the h-BN/Rh(111) surface, and iii) for applied sample biases large enough to promote charging. d) i–iii) nc-AFM images of the system for sample bias −1, −2, and −2.5 V (setpoint: 200 pA, excitation amplitude: 45 pm, Q-factor 13k). iv–vi) Laplace filtered nc-AFM images to increase contrast. Charging ring visible around central C_{60} (red arrows) for large enough sample bias.

Fermi energy. In step (iii), we apply a sample bias large enough in magnitude to populate LUMO and change the charge state of the central C_{60} by adding an electron. Importantly, the critical bias is not constant but scales inversely with the tip-sample distance, such that a critical electric field is reached. This dependency is studied *via* nc-AFM measurements presented in Figure 5d. A measurement for a sample bias smaller in magnitude than the required charging voltage is shown in Figure 5d-i. When the electric field of the tip is large enough to charge the central C_{60}, we can see a ring forming around the C_{60} in the pore center (Figure 5d-ii). Upon further increasing the sample bias, the tip can be further away from the central C_{60} resulting in a larger charging ring (Figure 5d-iii). To increase the contrast of the charging ring, we Laplace filtered the nc-AFM images (Figure 5e-iv–vi).

Charging rings, as we can see here, have also been observed in nc-AFM measurements of donor atoms or vacancies in semiconductors[46,47] and on fluorinated cobalt phthalocyanines on h-BN/Cu(111).[45] However, in both cases, the position of the charged impurity/molecule on the substrate was arbitrary.

Here the templating effect of the Moiré pattern determines that only C_{60} adsorbed in the pore center are subject to charge state changes.

3. Conclusion

In summary, we have studied the electronic properties of C_{60} molecules adsorbed on the h-BN/Rh(111) surface. Taking advantage of the commensurability between the hexagonal C_{60} lattice and the h-BN/Rh(111) Moiré, we could determine the adsorption-site dependent gating effect of the electrostatic surface potential on the LUMO of the C_{60}, leading to energetic shifts of up to 0.55 eV.

Comparing our experimental dI/dV spectra to tight-binding calculations allows us to investigate the role of the position-dependent energy level alignment on the hybridization of the C_{60} LUMO with neighboring molecules in the close-packed molecular islands and heptamers. We could identify C_{60} adsorbed in

the pore center to be mostly electronically decoupled from neighboring molecules. The lack of hybridization with neighboring molecules combined with the decoupling properties of the h-BN gives rise to the very sharp linewidth of the LUMO orbital in our dI/dV measurements of ≈ 70 meV. Furthermore, it allows us to observe a resonant electron-phonon scattering process, which has previously only been observed in off-resonant measurements.

Last, we use the combination of two gating mechanisms, namely the electrostatic surface potential and the electric field of the STM-tip, to promote and observe single molecular charging events. Changing the applied tip bias allows us to switch between charged and uncharged C_{60}. As such, a potential application could be seen in molecular electronics, where reliable molecular switches are a core element.[48]

In the case of C_{60}, both gating effects are needed to change the charge state. However, for bigger fullerenes like C_{70} or C_{84} with an intrinsically smaller electronic bandgap,[49] the gating of the STM-tip might not be necessary, providing a potential pathway to study regular arrays of intrinsically charged and uncharged fullerenes, as well as systems with more than one accessible charge state. Our results further develop the understanding of intermolecular hybridization, charge transfer, and electronic decoupling of molecules, which is crucial for future 2D material-organic hybrid applications.

4. Experimental Section

Sample Preparation: All sample preparation steps were performed in a UHV preparation chamber, operating at a base pressure in the mid 10^{-10} mbar range. First, the Rh(111) single crystal surface was cleaned via recurrent Ar^+ sputtering and annealing cycles at 850 °C. During sputtering, the crystal was kept at 500 °C to prevent argon inclusions. Next, h-BN monolayer growth was accomplished by decomposing borazine $(HBNH)_3$ gas on the 800 °C hot Rh(111) surface at 2×10^{-7} mbar for 10 min. Before dosing the gas into the preparation chamber, the borazine source was degassed by freeze-pump cycling three times. After decomposition, the crystal was annealed for 2 min and cooled down slowly to prevent defect formation. After degassing, the 99.95% pure C_{60} molecules (Sigma Aldrich) were sublimated at 430 °C from a quartz crucible onto the crystal surface held at around 100 °C to promote C_{60} island formation.

Measurements: Scanning probe measurements were performed in two commercial Scienta Omicron scanning probe microscopes: a low-temperature STM and a low-temperature STM with Q+ AFM. Experiments were conducted at a temperature of 4.5 K and UHV conditions with a base pressure in the low 10^{-10} mbar range. Two STM tips were used. A tungsten STM tip and an 80:20 Pt:Ir tip attached to a commercial Q+ tuning fork with a resonance frequency of 22.2 kHz. Clean Au(111) single crystals were used for tip forming.

All STM images were taken in constant current mode with the indicated setpoint values in the caption. dI/dV spectra were acquired via the lock-in technique at constant height mode with indicated values for the opening of the feedback loop and modulation voltage.

KPFS spectra and nc-AFM images were recorded in constant height mode in measuring the resonance frequency shift of a Pt:Ir tip attached to a Q+ sensor using Omicron Matrix Electronics and a Zurich Instruments HF2Li PLL. Excitation amplitude, Q-factor, and setpoint values before the opening of the feedback loop are indicated in the captions.

Tight-Binding Calculations: The tight-binding code for calculating the valence electronic structure of the C_{60} structures has been implemented according to the paper of N. Tit and V. Kumar.[50] The parametrization has been adjusted to match the density function theory results of a free-standing 2D-layer of C_{60} (with a 2×1 structure).[40] An excellent agree-

ment of the h_u, t_{1u}, and t_{2u} derived frontier bands was achieved with the following parameter set: $E_s = -6.7$ eV; $E_p = 0$ eV; $V_{ss\sigma} = -5.55$ eV; $V_{sp\sigma} = 5.31$ eV; $V_{pp\sigma} = +6.2$ eV and $V_{pp\pi} = -2.3$ eV. The distance dependence decay was parametrized with $L = 0.45$ Å and $d_0 = 1.54$ Å. Electrostatic potential variations $\Delta\phi_i$ of the ith C_{60} in the 2D layer were realized by adding $\Delta\phi_i$ to the on-site elements E_s and E_p of the orbitals belonging to the ith C_{60}. Additional information on parameters and band structure can be found in Figure S2, Supporting Information. Tight-binding calculations were performed in Wave Metrics Igor Pro 8.

Data Analysis: The presented data were processed with Wave Metrics Igor Pro 8 and WSxM.[51]

Supporting Information

Supporting Information is available from the Wiley Online Library or from the author.

Conflict of Interest

The authors declare no conflict of interest.

Data Availability Statement

The data that support the findings of this study are available from the corresponding author upon reasonable request.

[1] G. G. Naumis, in *Synthesis, Modelling and Characterization of 2D Materials and their Heterostructures* (Eds: E.-H. Yang, D. Datta, J. Ding, G. Hader), Elsevier, Amsterdam **2020**, pp. 77–109.

[2] G.-H. Lee, Y.-J. Yu, X. Cui, N. Petrone, C.-H. Lee, M. S. Choi, D.-Y. Lee, C. Lee, W. J. Yoo, K. Watanabe, T. Taniguchi, C. Nuckolls, P. Kim, J. Hone, *ACS Nano* **2013**, *7*, 7931.

[3] M. M. Furchi, F. Höller, L. Dobusch, D. K. Polyushkin, S. Schuler, T. Mueller, *npj 2D Mater. Appl.* **2018**, *2*, 3.

[4] J. Han, J. Wang, M. Yang, X. Kong, X. Chen, Z. Huang, H. Guo, J. Gou, S. Tao, Z. Liu, Z. Wu, Y. Jiang, X. Wang, *Adv. Mater.* **2018**, *30*, 1804020.

[5] G. J. Choi, Q. Van Le, K. S. Choi, K. C. Kwon, H. W. Jang, J. S. Gwag, S. Y. Kim, *Adv. Mater.* **2017**, *29*, 1702598.

**ADVANCED
SCIENCE NEWS**

www.advancedsciencenews.com

**ADVANCED
PHYSICS
RESEARCH**
Open Access

www.advphysicsres.com

[6] N. R. Glavin, C. Muratore, M. Snure, *Oxford Open Mater. Sci.* **2021**, *1*, itaa002.

[7] S. Parui, L. Pietrobon, D. Ciudad, S. Vélez, X. Sun, F. Casanova, P. Stoliar, L. E. Hueso, *Adv. Funct. Mater.* **2015**, *25*, 2972.

[8] J. Sun, Y. Choi, Y. J. Choi, S. Kim, J.-H. Park, S. Lee, J. H. Cho, *Adv. Mater.* **2019**, *31*, 1803831.

[9] N. S. Sariciftci, *Prog. Quantum Electron.* **1995**, *19*, 131.

[10] A. Nagashima, N. Tejima, Y. Gamou, T. Kawai, C. Oshima, *Phys. Rev. B* **1995**, *51*, 4606.

[11] C. Lee, S. Rathi, M. A. Khan, D. Lim, Y. Kim, S. J. Yun, D.-H. Youn, K. Watanabe, T. Taniguchi, G.-H. Kim, *Nanotechnology* **2018**, *29*, 335202.

[12] X. Han, J. Lin, J. Liu, N. Wang, D. Pan, *J. Phys. Chem. C* **2019**, *123*, 14797.

[13] A. F. Khan, E. P. Randviir, D. A. C. Brownson, X. Ji, G. C. Smith, C. E. Banks, *Electroanalysis* **2017**, *29*, 622.

[14] L. Liu, T. Dienel, R. Widmer, O. Gröning, *ACS Nano* **2015**, *9*, 10125.

[15] M. Corso, W. Auwärter, M. Muntwiler, A. Tamai, T. Greber, J. Osterwalder, *Science* **2004**, *303*, 217.

[16] S. Berner, M. Corso, R. Widmer, O. Groening, R. Laskowski, P. Blaha, K. Schwarz, A. Goriachko, H. Over, S. Gsell, M. Schreck, H. Sachdev, T. Greber, J. Osterwalder, *Angew. Chem., Int. Ed.* **2007**, *46*, 5115.

[17] A. B. Preobrajenski, S. A. Krasnikov, A. S. Vinogradov, M. L. Ng, T. Käämbre, A. A. Cafolla, N. Mårtensson, *Phys. Rev. B* **2008**, *77*, 085421.

[18] F. Schulz, R. Drost, S. K. Hämäläinen, P. Liljeroth, *ACS Nano* **2013**, *7*, 11121.

[19] H. Dil, J. Lobo-Checa, R. Laskowski, P. Blaha, S. Berner, J. Osterwalder, T. Greber, *Science* **2008**, *319*, 1824.

[20] S. Roth, T. Greber, J. Osterwalder, *ACS Nano* **2016**, *10*, 11187.

[21] R. Laskowski, P. Blaha, T. Gallauner, K. Schwarz, *Phys. Rev. Lett.* **2007**, *98*, 106802.

[22] A. B. Preobrajenski, M. A. Nesterov, M. L. Ng, A. S. Vinogradov, N. Mårtensson, *Chem. Phys. Lett.* **2007**, *446*, 119.

[23] T. Greber, M. Corso, J. Osterwalder, *Surf. Sci.* **2009**, *603*, 1373.

[24] P. A. Heiney, J. E. Fischer, A. R. McGhie, W. J. Romanow, A. M. Denenstein, J. P. McCauley Jr., A. B. Smith, D. E. Cox, *Phys. Rev. Lett.* **1991**, *66*, 2911.

[25] M. Grobis, X. Lu, M. F. Crommie, *Phys. Rev. B* **2002**, *66*, 161408.

[26] F. Rossel, M. Pivetta, F. Patthey, E. Ćavar, A. P. Seitsonen, W.-D. Schneider, *Phys. Rev. B* **2011**, *84*, 075426.

[27] L. Tang, Q. Guo, *Phys. Chem. Chem. Phys.* **2012**, *14*, 3323.

[28] G. Reecht, B. W. Heinrich, H. Bulou, F. Scheurer, L. Limot, G. Schull, *New J. Phys.* **2017**, *19*, 113033.

[29] M. Schaal, T. Aihara, M. Gruenewald, F. Otto, J. Domke, R. Forker, H. Yoshida, T. Fritz, *Beilstein J. Nanotechnol.* **2020**, *11*, 1168.

[30] Y. Ding, M. Iannuzzi, J. Hutter, *J. Phys. Chem. C* **2011**, *115*, 13685.

[31] T. R. Ohno, Y. Chen, S. E. Harvey, G. H. Kroll, J. H. Weaver, R. E. Haufler, R. E. Smalley, *Phys. Rev. B* **1991**, *44*, 13747.

[32] D. Porath, Y. Levi, M. Tarabiah, O. Millo, *Phys. Rev. B* **1997**, *56*, 9829.

[33] I. Fernández Torrente, K. J. Franke, J. Ignacio Pascual, *J. Phys.: Condens. Matter* **2008**, *20*, 184001.

[34] X. Lu, M. Grobis, K. H. Khoo, S. G. Louie, M. F. Crommie, *Phys. Rev. B* **2004**, *70*, 115418.

[35] J. Cho, J. Smerdon, L. Gao, Ö. Süzer, J. R. Guest, N. P. Guisinger, *Nano Lett.* **2012**, *12*, 3018.

[36] F. Schiller, M. Ruiz-Osés, J. E. Ortega, P. Segovia, J. Martínez-Blanco, B. P. Doyle, V. Pérez-Dieste, J. Lobo, N. Néel, R. Berndt, J. Kröger, *J. Chem. Phys.* **2006**, *125*, 144719.

[37] T. Frederiksen, K. J. Franke, A. Arnau, G. Schulze, J. I. Pascual, N. Lorente, *Phys. Rev. B* **2008**, *78*, 233401.

[38] K. J. Franke, J. I. Pascual, *J. Phys.: Condens. Matter* **2012**, *24*, 394002.

[39] D. J. Rizzo, Q. Dai, C. Bronner, G. Veber, B. J. Smith, M. Matsumoto, S. Thomas, G. D. Nguyen, P. R. Forrester, W. Zhao, J. H. Jørgensen, W. R. Dichtel, F. R. Fischer, H. Li, J.-L. Bredas, M. F. Crommie, *Nano Lett.* **2020**, *20*, 963.

[40] X. Cui, D. Han, H. Guo, L. Zhou, J. Qiao, Q. Liu, Z. Cui, Y. Li, C. Lin, L. Cao, W. Ji, H. Petek, M. Feng, *Nat. Commun.* **2019**, *10*, 3374.

[41] H. Guo, A. J. Martínez-Galera, J. M. Gómez-Rodríguez, *Nanotechnology* **2021**, *32*, 025711.

[42] K. Teichmann, M. Wenderoth, S. Loth, R. G. Ulbrich, J. K. Garleff, A. P. Wijnheijmer, P. M. Koenraad, *Phys. Rev. Lett.* **2008**, *101*, 076103.

[43] B. Schuler, D. Y. Qiu, S. Refaely-Abramson, C. Kastl, C. T. Chen, S. Barja, R. J. Koch, D. F. Ogletree, S. Aloni, A. M. Schwartzberg, J. B. Neaton, S. G. Louie, A. Weber-Bargioni, *Phys. Rev. Lett.* **2019**, *123*, 076801.

[44] N. Kocić, S. Decurtins, S.-X. Liu, J. Repp, *J. Chem. Phys.* **2017**, *146*, 092327.

[45] M. Pörtner, Y. Wei, A. Riss, K. Seufert, M. Garnica, J. V. Barth, A. P. Seitsonen, L. Diekhöner, W. Auwärter, *Adv. Mater. Interfaces* **2020**, *7*, 2000080.

[46] L. Cockins, Y. Miyahara, S. D. Bennett, A. A. Clerk, S. Studenikin, P. Poole, A. Sachrajda, P. Grutter, *Proc. Natl. Acad. Sci. U. S. A.* **2010**, *107*, 9496.

[47] W. Steurer, J. Repp, L. Gross, G. Meyer, *Surf. Sci.* **2018**, *678*, 112.

[48] J. L. Zhang, J. Q. Zhong, J. D. Lin, W. P. Hu, K. Wu, G. Q. Xu, A. T. S. Wee, W. Chen, *Chem. Soc. Rev.* **2015**, *44*, 2998.

[49] Y. Yang, F. Arias, L. Echegoyen, L. P. F. Chibante, S. Flanagan, A. Robertson, L. J. Wilson, *J. Am. Chem. Soc.* **1995**, *117*, 7801.

[50] N. Tit, V. Kumar, *J. Phys.: Condens. Matter* **1993**, *5*, 8255.

[51] I. Horcas, R. Fernández, J. M. Gómez-Rodríguez, J. Colchero, J. Gómez-Herrero, A. M. Baro, *Rev. Sci. Instrum.* **2007**, *78*, 013705.